Higher Executive Control Network Coherence Buffers Against Puberty-Related Increases in Internalizing Symptoms During the COVID-19 Pandemic

Supplemental Information

Supplemental Methods and Materials

Sample

We recruited 214 children and adolescents from 2013–2016 for a longitudinal study assessing the effects of early life stress (ELS) on psychobiological development throughout the course of puberty (1–3). Exclusion criteria included contraindications to MRI scanning (e.g., non-removable metal in/on the body, pregnancy, claustrophobia), a history of learning disability, neurological disorder, or any serious cognitive or physical challenges that might interfere with the ability to understand or complete procedures, non-fluency in English, and self-reported onset of menses for females (to ensure that adolescents were in early stages of puberty given the focus of the parent study on neurodevelopment throughout puberty). Participants and their parent(s)/legal guardian(s) signed assent and consent forms, respectively, to participate in this study, which was approved by the Stanford University Institutional Review Board. Participants were compensated for their time.

190 of 214 participants successfully underwent resting-state fMRI scanning at baseline (T1). One participant's data could not be preprocessed due to surface reconstruction issues, 13 participants were dropped due to excessive motion (based on visual inspection and/or greater than 20% of volumes flagged for > 0.5 mm framewise displacement), and four participants were dropped due to poor coverage of the brain, resulting in 172 participants with usable brain data. On

April 3, 2020, we emailed an invitation to the 214 participants who completed the T1 assessment to complete a COVID-19-related survey. 103 participants provided COVID-19 survey data, 86 of whom had usable resting-state fMRI from T1; one participant did not provide responses to the internalizing symptoms questionnaire. Thus, the total current sample consisted of 85 adolescents (49 females) ages 9-13 (M=11.29, SD=.92) at T1 and ages 13-19 (M=16.50, SD=1.28) at the COVID-19 assessment ("COVID-19 assessment" conducted between April 3, 2020- April 20, 2020, approximately 2.5-4.5 weeks after the start of the March 17, 2020 Bay Area shelter-in-place directive). The interval between the T1 and COVID-19 assessments ranged from 3.72 to 6.54 years (M=5.20, SD=.70). A flowchart of the assessments and time-points is presented in Figure S1. The 103 adolescents who completed the COVID-19 assessment did not differ from the 111 participants enrolled in the parent study who did not complete the COVID-19 assessment in age ($t(210)=1.06$, p=.29), sex ($\chi^2(1)=.01$, p=.99), or internalizing symptoms ($t(200)=1.85$, p=.07) at T1; however, participants who completed the COVID-19 assessment had lower ELS severity ($t(200)=3.00$, p=.004) and were in lower stages of puberty ($t(210)=2.36$, p=.02) at T1 compared to participants who did not complete the survey.

Cumulative early life stress severity (T1)

A modified version of the Traumatic Events Screening Inventory for Children (TESI-C) (4) was used to assess the impact of 30+ types of stressful life experiences (e.g., physical and emotional abuse, domestic violence). Interviewers asked adolescents to provide details about stressful life events in order to assess their severity and impact. Using a modified version of the UCLA Life Stress Interview coding system (6), three coders blind to the adolescent's subjective severity ratings then rated the objective severity of each event on a 5-point scale (0=non-impactful;

4=extremely severe impact). A cumulative ELS severity score was computed by summing the maximum objective severity scores for each type of endorsed stressor. Additional details on the scoring procedure and the range of cumulative ELS severity scores in the larger sample have been previously been reported (8), and the scoring algorithm is available at https://github.com/lucysking/els_stress_interview.

Scan data acquisition

Functional resting-state scan data were collected at the Stanford Center for Cognitive and Neurobiological Imaging using a 3T GE Discovery MR750 MRI scanner with a 32-channel head coil. Participants were given padding to minimize movement and earplugs to dampen scanner sounds. A series of 180 time points was acquired with an axial echo-planar imaging T2*-weighted sequence: echo time [TE]=30 ms; repetition time [TR]=2000 ms; isometric voxel size=3.2mm^3; slices=37 (interleaved acquisition); field of view [FOV]=224 mm; flip angle [FA]=77°; total scan time=6 min. The first five volumes were discarded to ensure magnet stabilization. During the resting-state scan, participants were instructed to lie still with their eyes open and to focus on a fixation cross on the screen. To register the functional images to anatomical space, a high-resolution T1-weighted structural scan was acquired using a sagittal spoiled gradient echo sequence (TE=2.34 ms; TR=6.24 ms; voxel size=0.8984 x 0.8984 x 0.9000 mm; slices=186; FOV=230 mm; FA=12°; total scan time=5:15 min).

Scan data preprocessing

Results included in this manuscript come from preprocessing conducted using fMRIPrep 1.5.0 (5), which is based on Nipype 1.2.2 (7,9).

Anatomical data preprocessing. The T1-weighted (T1w) image was corrected for intensity non-uniformity (INU) with N4BiasFieldCorrection (10), distributed with ANTs 2.2.0 (11) and used as T1w-reference throughout the workflow. The T1w-reference was then skull-stripped with a Nipype implementation of the antsBrainExtraction.sh workflow (from ANTs), using OASIS30ANTs as target template. Brain tissue segmentation of cerebrospinal fluid (CSF),white-matter (WM) and gray-matter (GM) was performed on the brain-extracted T1w using fast (12). Brain surfaces were reconstructed using recon-all (13), and the brain mask estimated previously was refined with a custom variation of the method to reconcile ANTs-derived and FreeSurfer-derived segmentations of the cortical gray-matter of Mindboggle (14). Volume-based spatial normalization to standard space (MNI152Lin) was performed through nonlinear registration with antsRegistration (ANTs 2.2.0), using brain-extracted versions of both T1w reference and the T1w template. The Linear ICBM Average Brain (ICBM152) Stereotaxic Registration Model ((15) TemplateFlow ID: MNI152Lin) was used for spatial normalization.

Functional data preprocessing. For the resting-state fMRI data, the following preprocessing was performed. First, a reference volume and its skull-stripped version were generated using a custom methodology of fMRIPrep. Based on the estimated susceptibility distortion, an unwarped BOLD reference was calculated for a more accurate co-registration with the anatomical reference. The BOLD reference was then co-registered to the T1w reference using bbregister (FreeSurfer) which implements boundary-based registration (16). Co-registration was configured with six degrees of freedom. Head-motion parameters with respect to the BOLD reference (transformation matrices, and six corresponding rotation and translation parameters) are estimated before any spatiotemporal filtering using mcflirt (FSL 5.0.9, (17)). BOLD runs were slice-time corrected using 3dTshift from AFNI 20160207 (18). The BOLD time-series, were resampled to surfaces in the fsaverage5 space.

The BOLD time-series were resampled onto their original, native space by applying a single, composite transform to correct for head-motion and susceptibility distortions. These resampled BOLD time-series will be referred to as "preprocessed BOLD". The BOLD time-series were resampled into the MNI152Lin standard space. First, a reference volume and its skull-stripped version were generated using a custom methodology of fMRIPrep. Several confounding time-series were calculated based on the preprocessed BOLD: framewise displacement (FD), DVARS and three region-wise global signals. FD and DVARS are calculated for each run, both using their implementations in Nipype (following the definitions by Power et al., (19)). The three global signals are extracted within the CSF, the WM, and the whole-brain masks. Additionally, a set of physiological regressors were extracted to allow for component-based noise correction (CompCor, (20)). Principal components are estimated after high-pass filtering the preprocessed BOLD time-series (using a discrete cosine filter with 128s cut-off) for the anatomical (aCompCor). A subcortical mask is obtained by heavily eroding the brain mask, which ensures it does not include cortical GM regions. For aCompCor, components are calculated within the intersection of the aforementioned mask and the union of CSF and WM masks calculated in T1w space, after their projection to the native space of each functional run (using the inverse BOLD-to-T1w transformation). Components are also calculated separately within the WM and CSF masks. For each CompCor decomposition, the k components with the largest singular values are retained, such that the retained components' time series are sufficient to explain 50 percent of variance across the nuisance mask (CSF, WM, or combined). The remaining components are dropped from consideration. The head-motion estimates calculated in the correction step were also placed within the corresponding confounds file. The confound time series derived from head motion estimates and global signals were expanded with the inclusion of temporal derivatives and quadratic terms

for each (21). Frames that exceeded a threshold of 0.5 mm FD or 1.5 standardised DVARS were annotated as motion outliers. All resamplings can be performed with a single interpolation step by composing all the pertinent transformations (i.e. head-motion transform matrices, susceptibility distortion correction when available, and co-registrations to anatomical and output spaces). Gridded (volumetric) resamplings were performed using antsApplyTransforms (ANTs), configured with Lanczos interpolation to minimize the smoothing effects of other kernels (22). Non-gridded (surface) resamplings were performed using mri_vol2surf (FreeSurfer).

Following preprocessing in *fMRIPrep*, the first 5 frames were discarded to allow the MR signal to achieve T1 equilibrium. We then conducted nuisance regression followed by temporal band-pass filtering (.01 - .1 Hz) to the resting-state data. Our nuisance regressors included framewise displacement, translation and rotation (x,y,z) and their first and second derivatives, and aCompCor components 0-5.

Supplemental Results

Correlations Among Self-Report Variables

Pubertal stage at T1 was positively correlated with age at the T1 ($r(83)=.23$, $p=.03$) and COVID-19 assessments ($r(83)=.32$, $p=.003$). By design, males and females did not differ in pubertal staging at T1, $F(83)=1.55$, $p=.22$. Although there was no significant association between pubertal stage and internalizing symptoms at T1 ($p=.36$), a regression analysis testing sex differences in the association between these variables yielded a significant interaction of sex and pubertal stage ($F(79)=4.94$, $p=.029$): whereas females showed a positive relation between pubertal stage and internalizing symptoms at T1 ($t(34)=2.11$, $p=.038$), males did not ($t(47)=-1.15$, $p=.26$). While there was no significant association between pubertal stage and internalizing severity pre-COVID-19 ($p=.28$), pubertal stage was positively associated with internalizing severity peri-COVID-19 ($r(83)=.22$, $p=.04$). Internalizing symptoms at T1 were correlated with pre-COVID-19 internalizing severity ($r(83)=.21$, $p=.05$), but not with peri-COVID-19 internalizing severity ($p=.36$). While there were no sex differences in internalizing severity at T1 ($p=.11$), females reported greater internalizing severity during pre-COVID-19 ($t(83)=2.37$, $p=.02$) and peri-COVID-19 ($t(83)=3.77$, $p<.01$) than did males. Females, but not males, exhibited a positive association between ELS and pubertal stage ($t(47)=2.25$, $p=.027$, and $t(34)=-1.53$, $p=.13$, respectively; Full Model: $t(80)=2.71$, $p=.008$).

Tests of Associations between ECN Coherence and Model Covariates

We tested whether bilateral ECN coherence was related to our model covariates. Although bilateral ECN coherence was not significantly associated with sex, age (T1 or COVID-19), pubertal stage (T1), internalizing problems (T1), or SES (T1) (all ps>.05), ECN coherence was

negatively associated with ELS at T1 ($r(83)=-.25$, $p=.022$). This finding is consistent with prior literature showing that childhood abuse is associated with deficits in executive functioning and lower connectivity among ECN regions (23). Similarly, previous research has shown that adolescent girls who experienced ELS have an earlier onset of pubertal maturation and age of menarche (24). We tested whether this is true in our sample using a regression analysis including pubertal stage as a dependent variable, sex and ELS as an interaction term, and age as a covariate. Indeed, females, but not males, in our sample exhibited a positive association between ELS and pubertal stage ($t(47)=2.25$, $p=.027$, and $t(34)=-1.53$, $p=.13$, respectively; Full Model: $t(80)=2.71$, $p=.008$). Thus, ELS may contribute to both earlier pubertal maturation and lower ECN coherence in females; the combination of lower ECN coherence and more advanced pubertal staging relative to peers may exacerbate their internalizing symptoms during periods of stress, such as the COVID-19 pandemic.

Sensitivity Analyses

To test whether other networks, such as the SN and DMN, might similarly moderate the association between more advanced pubertal staging at T1 and increases in internalizing severity from pre- to peri-COVID-19, we replaced the ECN variable with the DMN and SN in two additional regression models. There was no significant main effect of the DMN or interaction with pubertal stage on the difference between pre- and peri-COVID-19 internalizing severity, ($p=.08$ and .11, respectively, for main and interaction effects; Table S2). In addition, there was no main effect of the SN ($p=.66$) or interaction with pubertal stage on the difference between pre- and peri-COVID-19 internalizing severity ($p=.73$; Table S3).

We also tested whether the left or right ECN differentially modulates the association between pubertal stage and changes in internalizing symptoms during COVID-19 by modeling two interaction terms in one regression model (right ECN x pubertal stage, and left ECN x pubertal stage). This analysis indicated that only the left ECN moderated the association between puberty and internalizing symptom changes ($t(63)=-2.25$, $p=.01$); the right ECN did not ($p=.10$; Table S4).

Finally, to test whether our main results (described in section 3.2) were driven by females in the sample, we reran our model and included a third interaction term (i.e., sex X pubertal stage X ECN). Interestingly, we found that the three-way interaction of these variables was significant ($t(62)=2.14$, $p=.04$). Simple slopes analyses again showed that in females, the positive association between pubertal stage and the difference in internalizing severity from pre- to peri-COVID-19 was significant when bilateral ECN coherence was low ($\beta=.44$, $p=.03$), but not when ECN coherence was high ($\beta=.04$, $p=.79$). In contrast, males showed a positive association between pubertal stage and increase in internalizing severity from pre- to peri-COVID-19 when ECN coherence was low ($\beta=.85$, $p<.01$), but a *negative* association between pubertal stage and internalizing changes when ECN coherence was high ($\beta=-.56$, $p=.03$). Specifically, males with higher ECN coherence who were in more advanced stages of puberty at T1 exhibited a decrease in internalizing severity during the pandemic (Table S5; Figure S5). While these results are interesting and suggest a more protective role of the ECN in early developing males compared to females, they should be interpreted with caution given the relatively small cell sizes when conducting a three-way interaction.

Supplemental Figures and Tables

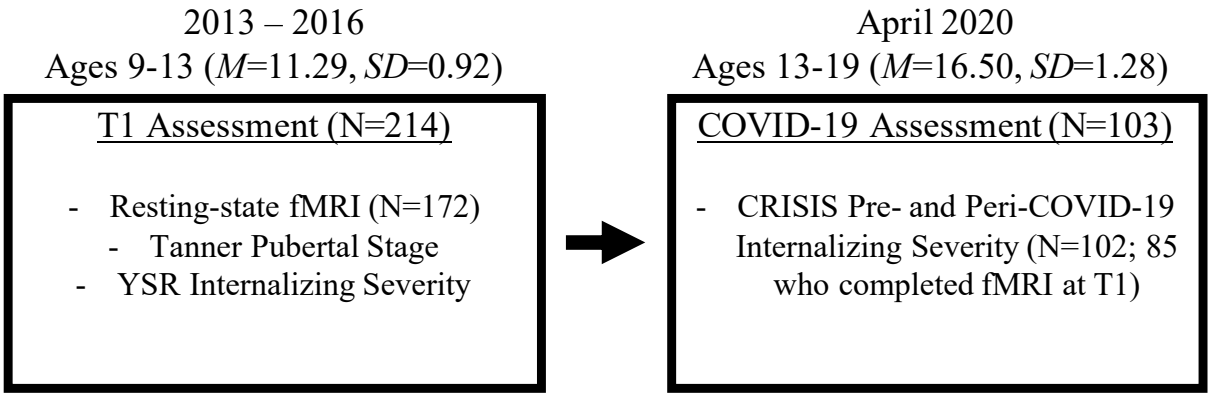

Figure S1. Flowchart of sample recruitment and assessment time-points.

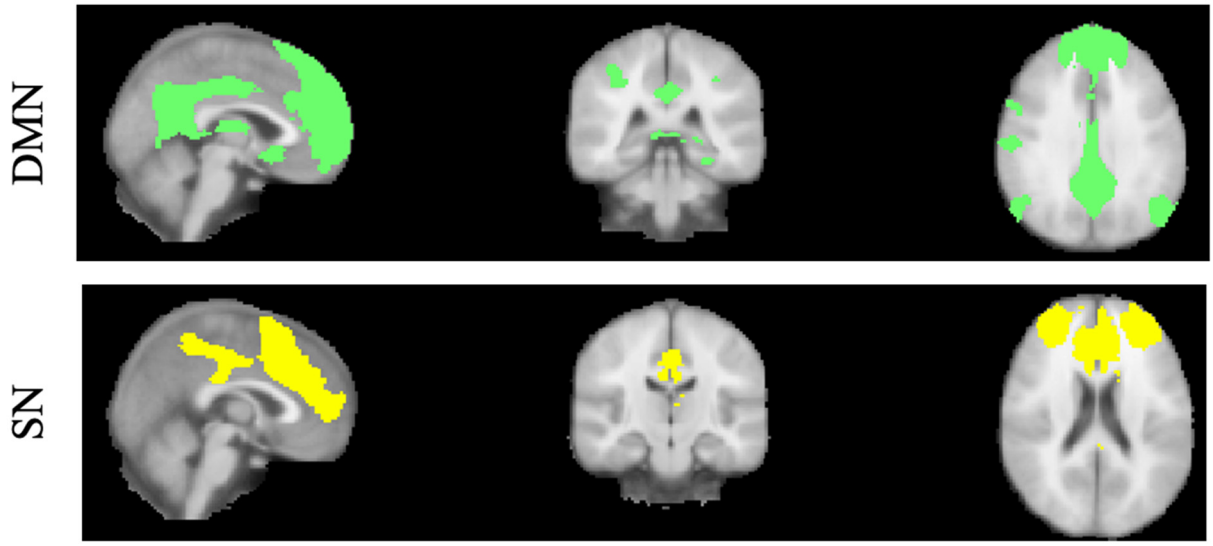

Figure S2. Default-mode (DMN) and salience (SN) networks identified using ICA.

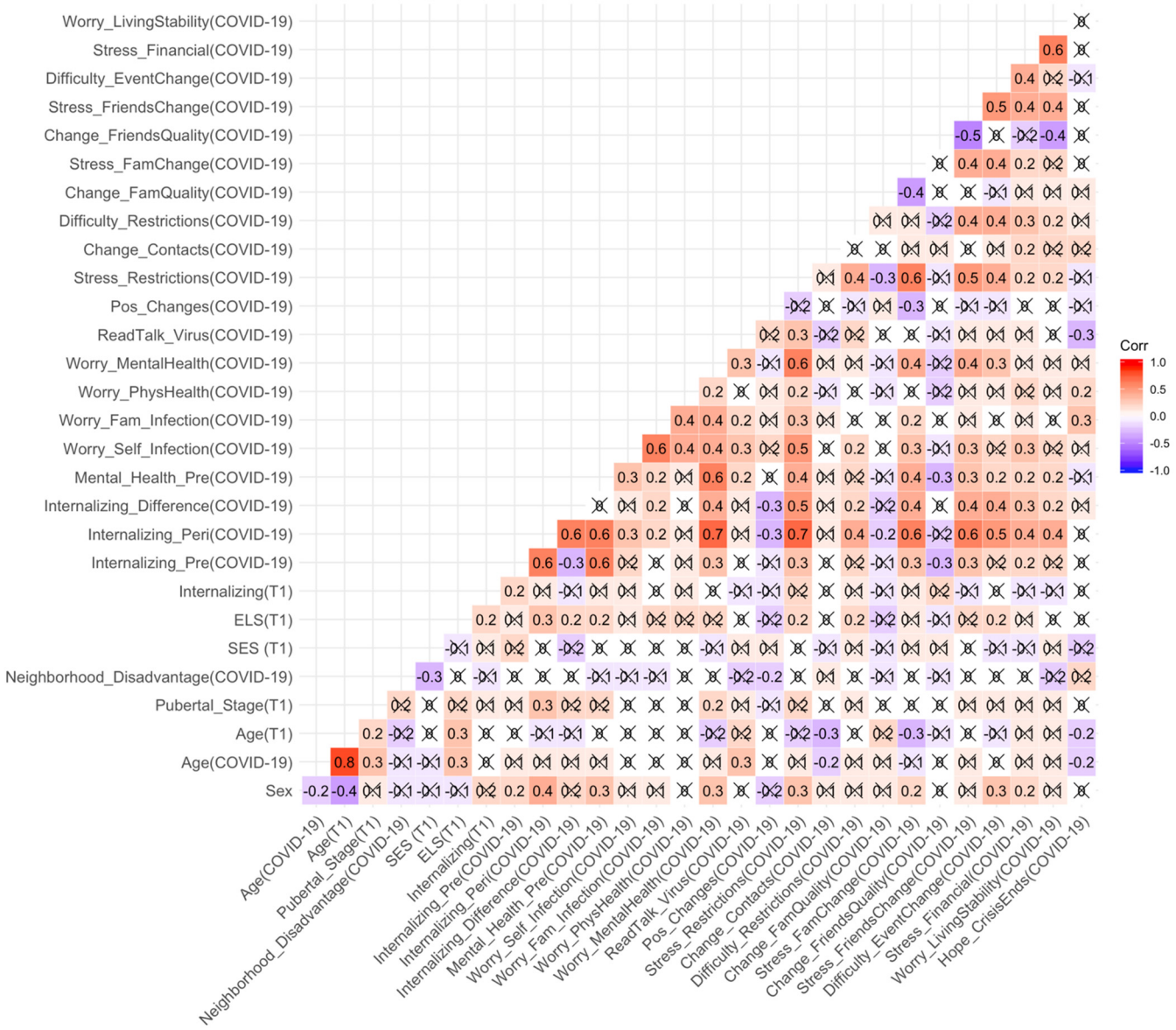

Figure S3. Correlations among study variables. "X" indicates non-significant correlations (p>.05).

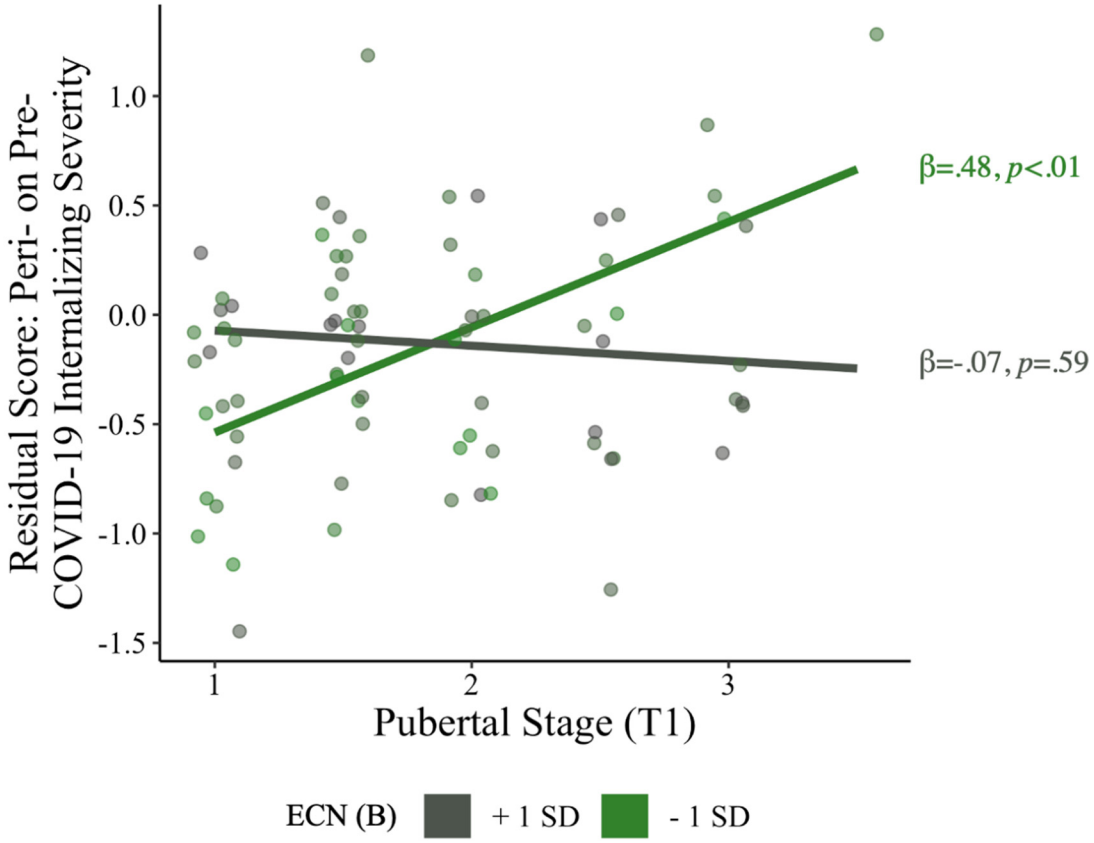

Figure S4. ECN coherence moderates the association between early pubertal maturation and residual scores of peri-COVID-19 regressed on pre-COVID-19 internalizing severity.

Note: ECN (B)=bilateral executive control network coherence. Pubertal stage is relative to same-age peers. ECN is only grouped (Mean +1 SD/ - 1 SD) for visualization. The regression model included the interaction of pubertal stage (T1) and ECN (T1; both continuous variables) and the following covariates: age (T1 and COVID-19), internalizing severity (T1), sex, ELS severity (T1), head motion during the scan (i.e., mean frame-wise displacement), an identified "noise" component from the ICA (T1), as well as SES and neighborhood disadvantage (T1).

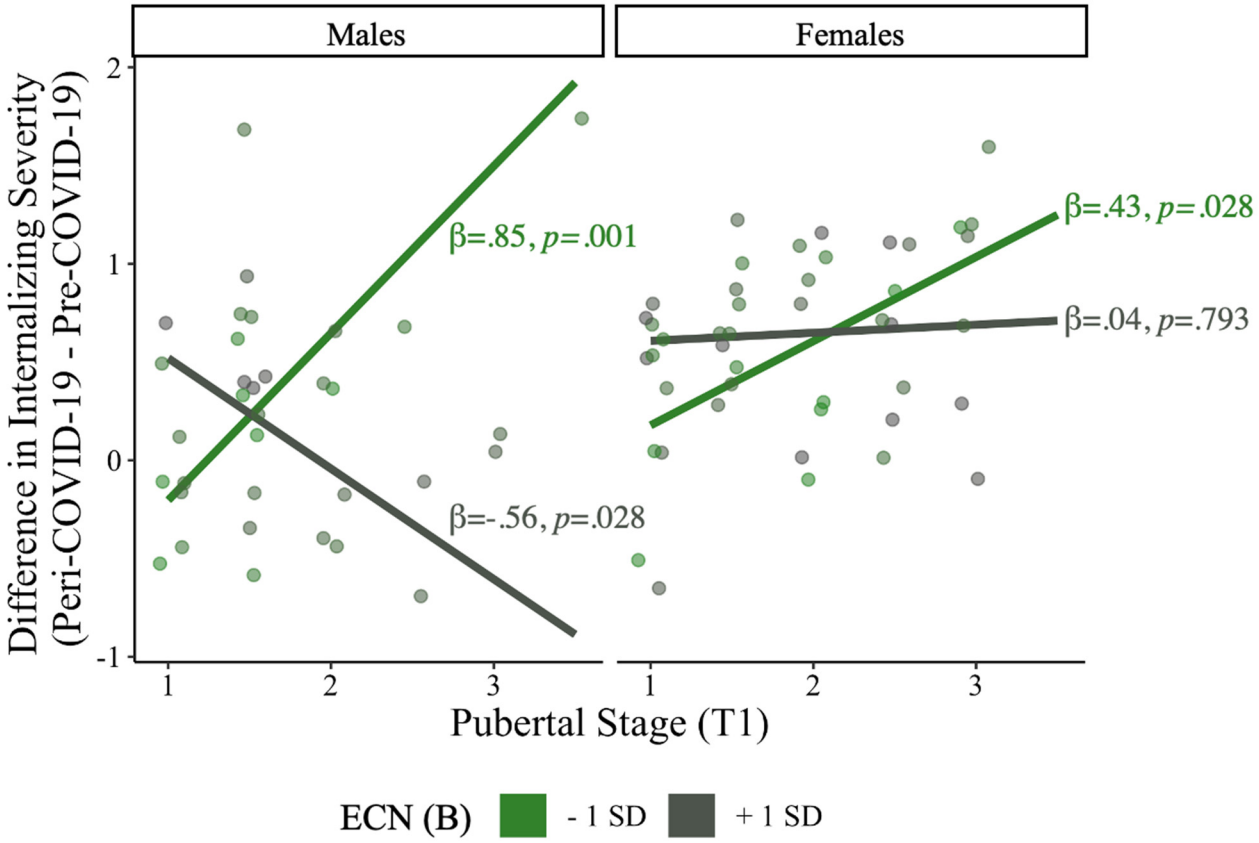

Figure S5. Sex differences in the effects of ECN coherence on the association between early pubertal maturation and differences in reported pre- to peri-COVID-19 internalizing severity.

Note: ECN (B)=bilateral executive control network coherence. Pubertal stage is relative to same-age peers. ECN is only grouped (Mean +1 SD/ - 1 SD) for visualization. The regression model included the interaction of sex, pubertal stage (T1), and ECN (T1) and the following covariates: age (T1 and COVID-19), internalizing severity (T1 and pre-COVID-19), sex, ELS severity (T1), head motion during the scan (i.e., mean frame-wise displacement), an identified "noise" component from the ICA (T1), as well as SES and neighborhood disadvantage (T1).

Table S1. Effects of pubertal stage and ECN coherence (T1) on residual score of peri-COVID-19 regressed on pre-COVID-19 internalizing severity.

Effect	*B*	*SE*	*t*	*p*
Pubertal Stage (T1)	0.23	0.12	1.90	.060
ECN (B) (T1)	-0.08	0.13	-0.67	.510
Scan Noise (T1)	-0.11	0.10	-1.11	.274
Age (COVID-19)	0.38	0.22	1.72	.090
Sex	0.48	0.22	2.12	.037
Head Motion During Scan (T1)	-0.25	-0.27	-0.93	.354
ELS Severity (T1)	0.49	0.15	3.38	.001
Neighborhood Disadvantage (COVID-19)	-0.16	0.11	-1.42	.161
Internalizing Symptoms (T1)	-0.22	0.11	-1.91	.061
Age (T1)	-0.52	0.19	-2.25	.028
SES/ Income to Needs (T1)	-0.02	0.13	-0.19	.848
Pubertal Stage X ECN (B)	-0.35	0.12	-2.85	.006
Simple Slopes of Pubertal Stage:				
ECN (B) – 1SD	0.57	0.18	3.22	.002
ECN (B) + 1SD	-0.08	0.15	-0.54	.594

Note: ECN (B) = bilateral executive control network coherence; ELS = Early life stress; SES = socioeconomic status. Head motion based on mean framewise displacement (mm) during scan. Beta estimates are standardized. Beta estimates are standardized.

Table S2. Effects of pubertal stage and DMN coherence (T1) on internalizing severity differences between pre- and peri-COVID-19.

Effect	*β*	*SE*	*t*	*p*
Pubertal Stage (T1)	-0.56	0.48	-1.18	.242
DMN (T1)	-1.39	0.77	-1.79	.078
Scan Noise (T1)	-0.47	0.44	-1.07	.289
Internalizing Severity (Pre-COVID-19)	-0.47	0.10	-4.56	.000
Age (COVID-19)	0.20	0.10	2.06	.043
Sex	0.35	0.15	2.40	.019
Head Motion During Scan (T1)	-0.48	1.02	-0.47	.642
ELS Severity (T1)	0.06	0.02	3.64	.001
Neighborhood Disadvantage (COVID-19)	0.00	0.00	-1.21	.229
Internalizing Symptoms (T1)	-0.01	0.01	-1.81	.075
Age (T1)	-0.39	0.14	-2.75	.008
SES/ Income to Needs (T1)	0.03	0.15	0.19	.848
Pubertal Stage X DMN	0.67	0.42	1.60	.114

Note: DMN=default mode network coherence

Table S3. Effects of pubertal stage and SN coherence (T1) on internalizing severity differences between pre- and peri-COVID-19.

Effect	*β*	*SE*	*t*	*p*
Pubertal Stage (T1)	0.33	0.44	0.74	.459
SN (T1)	0.37	0.84	0.44	.661
Scan Noise (T1)	-0.55	0.46	-1.19	.236
Internalizing Severity (Pre-COVID-19)	-0.49	0.11	-4.53	.000
Age (COVID-19)	0.21	0.10	2.12	.038
Sex	0.37	0.16	2.36	.021
Head Motion During Scan (T1)	-0.60	1.05	-0.57	.568
ELS Severity (T1)	0.06	0.02	3.46	.001
SES (COVID-19)	0.00	0.00	-1.07	.289
Internalizing Symptoms (T1)	-0.01	0.01	-1.58	.120
Age (T1)	-0.35	0.14	-2.45	.017
Income to Needs (T1)	0.03	0.16	0.18	.858
Pubertal Stage X SN	-0.15	0.44	-0.35	.731

Note: SN=salience network coherence.

Table S4. Effects of pubertal stage and ECN coherence (left and right; T1) on internalizing severity differences between pre- and peri-COVID-19.

Effect	*β*	*SE*	*t*	*p*
Pubertal Stage (T1)	0.22	0.10	2.09	.041
ECN (R) (T1)	0.01	0.10	0.06	.956
ECN (L) (T1)	0.00	0.10	0.00	.999
Scan Noise (T1)	-0.11	0.10	-1.07	.287
Internalizing Severity (Pre-COVID-19)	-0.44	0.10	-4.53	.000
Age (COVID-19)	0.37	0.19	1.92	.059
Sex	0.49	0.22	2.21	.031
Head Motion During Scan (T1)	-0.08	0.10	-0.87	.387
ELS Severity (T1)	0.34	0.11	3.24	.002
SES (COVID-19)	-0.12	0.10	-1.16	.251
Internalizing Symptoms (T1)	-0.16	0.10	-1.64	.106
Age (T1)	-0.45	0.19	-2.37	.021
Income to Needs (T1)	0.01	0.10	0.05	.961
Pubertal Stage X ECN (R)	-0.16	0.10	-1.65	.104
Pubertal Stage X ECN (L)	-0.25	0.10	-2.52	.014

Note: ECN=executive control network coherence; (R)=right; (L)=left.

Table S5. Sex differences in the effect of ECN coherence on the association between pubertal stage and internalizing severity differences between pre- and peri-COVID-19.

Effect	*β*	*SE*	*t*	*p*
Pubertal Stage (T1)	0.12	0.16	0.75	.459
ECN (B) (T1)	-0.60	0.25	-2.46	.017
Scan Noise (T1)	-0.16	0.09	-1.63	.108
Internalizing Severity (Pre-COVID-19)	-0.39	0.09	-4.23	.001
Age (COVID-19)	0.40	0.22	1.88	.065
Sex	0.54	0.23	2.37	.021
Head Motion During Scan (T1)	-0.26	0.25	-1.04	.302
ELS Severity (T1)	0.49	0.14	3.53	.001
Neighborhood Disadvantage (COVID-19)	-0.14	0.10	-1.34	.184
Internalizing Symptoms (T1)	-0.17	0.11	-1.53	.132
Age (T1)	-0.51	0.22	-2.36	.022
SES/ Income to Needs (T1)	0.03	0.12	0.20	.840
Pubertal Stage X ECN (B)	-0.88	0.26	-3.41	.001
Sex X Pubertal Stage	0.14	0.21	0.64	.530
Sex X ECN (B)	0.63	0.28	2.29	.025
Sex X ECN (B) X Pubertal Stage	0.64	0.28	2.29	.036
Males	-0.06	0.13	-0.49	.630
ECN (B) – 1SD	0.97	0.29	3.38	.001
ECN (B) + 1SD	-0.64	-.29	-2.26	.028
Females				
ECN (B) – 1SD	0.49	0.22	2.25	.028
ECN (B) + 1SD	.047	0.18	0.26	.793

Note: ECN (B) = bilateral executive control network coherence; ELS = Early life stress; SES = socioeconomic status. Head motion based on mean framewise displacement (mm) during scan. Beta estimates are standardized.

Supplemental References

1. Humphreys KL, Kircanski K, Colich NL, Gotlib IH (2016): Attentional avoidance of fearful facial expressions following early life stress is associated with impaired social functioning. *J Child Psychol Psychiatry* 57: 1174–1182.

2. King LS, Humphreys KL, Camacho MC, Gotlib IH (2019): A person-centered approach to the assessment of early life stress: Associations with the volume of stress-sensitive brain regions in early adolescence. *Development and Psychopathology* 31: 643–655.

3. Miller JG, Ho TC, Humphreys KL, King LS, Foland-Ross LC, Colich NL, *et al.* (2020): Early Life Stress, Frontoamygdala Connectivity, and Biological Aging in Adolescence: A Longitudinal Investigation. *Cereb Cortex*. https://doi.org/10.1093/cercor/bhaa057

4. Ribbe D (1996): Psychometric review of Traumatic Events Screening Inventory for Children (TESI-C). *Measurement of Stress, Trauma, and Adaptation*. Lutherville, MD: Sidran.

5. Esteban O, Markiewicz CJ, Blair RW, Moodie CA, Isik AI, Erramuzpe A, *et al.* (2019): fMRIPrep: a robust preprocessing pipeline for functional MRI. *Nature Methods* 16: 111–116.

6. Rudolph KD, Hammen C, Burge D, Lindberg N, Herzberg D, Daley SE (2000): Toward an interpersonal life-stress model of depression: The developmental context of stress generation. *Development and Psychopathology* 12: 215–234.

7. Gorgolewski K, Burns CD, Madison C, Clark D, Halchenko YO, Waskom ML, Ghosh SS (2011): Nipype: A Flexible, Lightweight and Extensible Neuroimaging Data Processing Framework in Python. *Front Neuroinform* 5. https://doi.org/10.3389/fninf.2011.00013

8. King LS, Colich NL, LeMoult J, Humphreys KL, Ordaz SJ, Price AN, Gotlib IH (2017): The Impact of the Severity of Early Life Stress on Diurnal Cortisol: The Role of Puberty. *Psychoneuroendocrinology* 77: 68–74.

9. Esteban O, Markiewicz CJ, Johnson H, Ziegler E, Manhães-Savio A, Jarecka D, *et al.* (2020): *Nipy/Nipype: 1.4.2*. Zenodo. https://doi.org/10.5281/zenodo.3668316

10. Tustison NJ, Avants BB, Cook PA, Zheng Y, Egan A, Yushkevich PA, Gee JC (2010): N4ITK: Improved N3 Bias Correction. *IEEE Transactions on Medical Imaging* 29: 1310–1320.

11. Avants BB, Epstein CL, Grossman M, Gee JC (2008): Symmetric diffeomorphic image registration with cross-correlation: Evaluating automated labeling of elderly and neurodegenerative brain. *Medical Image Analysis* 12: 26–41.

12. Zhang Y, Brady M, Smith S (2001): Segmentation of brain MR images through a hidden Markov random field model and the expectation-maximization algorithm. *IEEE Transactions on Medical Imaging* 20: 45–57.

13. Dale AM, Fischl B, Sereno MI (1999): Cortical Surface-Based Analysis: I. Segmentation and Surface Reconstruction. *NeuroImage* 9: 179–194.

14. Klein A, Ghosh SS, Bao FS, Giard J, Häme Y, Stavsky E, *et al.* (2017): Mindboggling morphometry of human brains. *PLoS Comput Biol* 13: e1005350.

15. Mazziotta JC, Toga AW, Evans A, Fox P, Lancaster J (1995): A Probabilistic Atlas of the Human Brain: Theory and Rationale for Its Development: The International Consortium for Brain Mapping (ICBM). *NeuroImage* 2: 89–101.

16. Greve DN, Fischl B (2009): Accurate and robust brain image alignment using boundary-based registration. *NeuroImage* 48: 63–72.

17. Jenkinson M, Bannister PR, Smith SM (2002): Improved Optimization for the Robust and Accurate Linear Registration and Motion Correction of Brain Images. *NeuroImage* 17: 825–841.

18. Cox RW (1996): AFNI: Software for Analysis and Visualization of Functional Magnetic Resonance Neuroimages. *Computers and Biomedical Research* 29: 162–173.

19. Power JD, Mitra A, Laumann TO, Snyder AZ, Schlaggar BL, Petersen SE (2014): Methods to detect, characterize, and remove motion artifact in resting state fMRI. *NeuroImage* 84: 320–341.

20. Behzadi Y, Restom K, Liau J, Liu TT (2007): A component based noise correction method (CompCor) for BOLD and perfusion based fMRI. *NeuroImage* 37: 90–101.

21. Satterthwaite TD, Elliott MA, Gerraty RT, Ruparel K, Loughead J, Calkins ME, *et al.* (2013): An improved framework for confound regression and filtering for control of motion artifact in the preprocessing of resting-state functional connectivity data. *NeuroImage* 64: 240–256.

22. Lanczos C (1964): Evaluation of Noisy Data. *Journal of the Society for Industrial and Applied Mathematics* Series B: 76–85.

23. Hart H, Lim L, Mehta MA, Chatzieffraimidou A, Curtis C, Xu X, *et al.* (2017): Reduced functional connectivity of fronto-parietal sustained attention networks in severe childhood abuse. *PLoS ONE* 12: e0188744.

24. Mendle, Leve LD, Van Ryzin M, Natsuaki MN, Ge X (2011): Associations Between Early Life Stress, Child Maltreatment, and Pubertal Development Among Girls in Foster Care. *Journal of Research on Adolescence* 21: 871–880.